Pergamon

Acta Astronautica Vol. 40, No. 12, pp. 859–869, 1997

Printed in Great Britain
0094-5765/98 $19.00+0.00

PII: S0094-5765(97)00128-8

NUMERICAL SIMULATION OF SPACE DEBRIS IMPACTS ON THE WHIPPLE SHIELD†

M. KATAYAMA[1], S. TODA[2] and S. KIBE[2]

[1]Engineering Solution Department, CRC Research Institute, Inc., 2-7-5, Minamisuna, Koto-ku, Tokyo, 136, Japan and [2]Structural Mechanics Division, National Aerospace Laboratory, 7-44-1, Jindaiji Higashi-machi, Chofu-shi, Tokyo, 182, Japan

(Received 31 January 1996)

Abstract—The authors carried out three series of experimental tests of the first bumper perforation and main wall cratering processes directly caused by three types of projectiles with about 2, 4 and 7 km s^{-1} impact velocities but comparable initial kinetic energies, by using three different accelerators (one-stage powder gun, two-stage light-gas gun and rail gun), for the purpose of investigating space debris hypervelocity impacts onto single-walled Whipple bumper shields [1]. In the present study, after reviewing the numerical simulation method of hydrocode for both Eulerian and Lagrangian descriptions, a number of parametric numerical simulation analyses using multiple material Eulerian methods were performed in order to optimize the material properties of bumper and main wall materials through comparison with experimental results of single target impacts by the projectiles. In particular, the material data on the dynamic fracture phenomena are discussed in detail in the first part.

Then a couple of numerical calculations using the interactive Lagrangian rezoning method to simulate the overall impact process against the single walled Whipple shield were performed and compared with the corresponding experimental results. Both results indicated fairly good agreement with each other. Moreover, it was demonstrated that the present method is helpful and efficient in understanding the impact phenomena and fracture mechanism in the space debris hypervelocity impact problem.

Finally the multiple material Eulerian method was applied to the same problems modeled by the interactive Lagrangian rezoning method used previously, because the former is much easier to use for almost all users, although it is more diffusive and unclear of material boundaries than the latter. Those two kinds of numerical results also indicated fairly good agreements with each other. © 1998 Published by Elsevier Science Ltd

1. INTRODUCTION

As the activities of mankind in space have increased, space debris has become a greater threat to our space development. Since the velocity of an orbital object in low Earth orbit (LEO) is about 7.5 km s^{-1}, the maximum relative impact velocity comes to about 15 km s^{-1}. Taking account of the angle of orbit crossing, the average relative impact velocity is estimated to be about 10 km s^{-1}. If an orbital space debris impacts a spacecraft at such a hypervelocity, the structure will be vaporized as well as perforated. The Whipple bumper shield, a single bumper walled double structure protection system, is adopted widely for this reason.

The authors proposed a simulation method to predict the bumper perforation and main wall cratering process of the Whipple bumper system caused by 10 km s^{-1} debris impact [2, 3]. Although it was a direct simulation method using a hydrocode including shock-induced vaporization phenomena, no experimental test facilities are available to verify these calculation conditions at present. However, since the proposed method is applicable to the hyper- or high-velocity impact region lower than 10 km s^{-1} impact velocity, it is of great importance to compare and verify the results of the calculation and the experiment. In particular, it is pointed out that the fragmentation of the bumper material might affect the damage of the main wall much more severely than the vaporization of it. Therefore, the above-mentioned investigation is significant from the viewpoint of the overall protection assessment of spacecraft from space debris.

2. EXPERIMENTAL FACILITIES AND CONDITIONS

Three types of launcher systems were used in order to accelerate the projectiles to three different impact velocities, but with comparable kinetic energies. The first is a one-stage powder gun of Kyoto Univ. shown in Fig. 1, the second is a two-stage light-gas gun of Tohoku Univ. shown in Fig. 2 and the last is a rail gun of the Institute of Space and Astronautical Science (ISAS) shown in Fig. 3. The first system has the ability to accelerate a 14 g high density polyethylene projectile up to about 2.2 km s^{-1}, the

---

†Paper IAF 95.I5.02 presented at the 46th International Astronautical Congress, Oslo, Norway, 2–6 October, 1995.

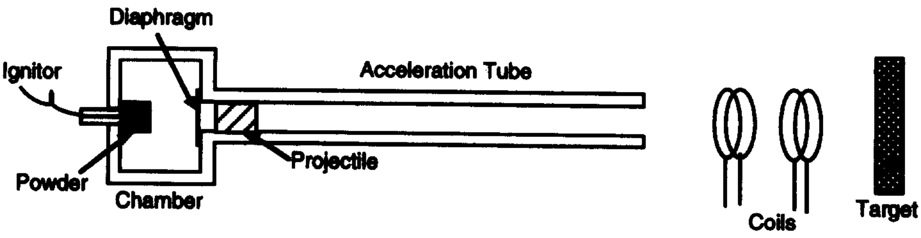

Fig. 1. Schematic diagram of one-stage powder gun accelerator system.

second takes a 3.7 g high density polyethylene projectile up to about 4.0 km s^{-1} and the last takes a 1 g polycarbonate projectile up to about 7.5 km s^{-1}. Consequently, all the projectiles which were accelerated by using these three types of guns have comparable initial kinetic energies. The impact velocity of every type of accelerator was measured by the average velocity measurement method. In the case of the powder gun, the electromagnetic induction was applied utilizing a magnet embedded in the tail of the projectile and two spaced coils along the trajectory. In the case of the two-stage light-gas gun, two thin wires insulated on the papers generate a trigger pulse by interruption of the projectile. Two X-ray scintillation probes placed a short distance downrange were used to measure the peak time delay of the passing projectile in the case of the rail gun. The final perforation and deformation profiles were measured by using an X-ray CT scanning system without cutting the specimens mechanically for every experiment.

For both bumper and main wall materials, 2024-T3 aluminum plates were adopted in this design. As target plates five different thickness plates were used: 2.5, 4.8, 12.7, 22.2 and 38.9 mm.

3. NUMERICAL APPROACH

For the purpose of analyzing hypervelocity impact phenomena, a so-called hydrocode is used generally. It was originally formulated as HEMP code by Wilkins in the 1950s [4]. The governing fundamental equations are based upon classical continuum mechanics, which describe the dynamic behavior of a continuous medium with a set of partial differential equations established through the conservation laws of (1) mass, (2) linear momentum and (3) energy. The equation of state and constitutive equation describing material properties are solved simultaneously together with those for the specified initial and boundary conditions. Many hydrocodes have adopted a finite difference scheme such as the HEMP code, and numerous hydrocodes have been formulated in the finite element method. Almost all of them are based upon an explicit time integration scheme in order to solve extremely transient phenomena.

As is well known, there are two ways to describe the above-mentioned fundamental equations: the Lagrangian (material) and Eulerian (spatial) description methods. The conservation equations of mass, momentum and energy for the two methods are as follows:Lagrangian description

$$\frac{D\rho}{Dt} + \rho\frac{\partial u_i}{\partial x_i} = 0 \tag{1-1}$$

$$\frac{Du_i}{Dt} = f_i + \frac{1}{\rho}\frac{\partial \sigma_{ji}}{\partial x_j} \tag{1-2}$$

$$\frac{De}{Dt} = f_i u_i + \frac{1}{\rho}\frac{\partial}{\partial x_j}(\sigma_{ij}u_i) \tag{1-3}$$

Eulerian description

$$\frac{\partial \rho}{\partial t} + \frac{\partial}{\partial x_i}(\rho u_i) = 0 \tag{2-1}$$

$$\frac{\partial u_i}{\partial t} + u_j\frac{\partial u_i}{\partial x_j} = f_i\frac{1}{\rho}\frac{\partial \sigma_{ij}}{\partial x_j} \tag{2-2}$$

$$\frac{\partial e}{\partial t} + u_i\frac{\partial e}{\partial x_i} = f_i u_i + \frac{1}{\rho}\frac{\partial}{\partial x_j}(\sigma_{ij}u_i) \tag{2-3}$$

where ρ is the mass density, x_i a spatial coordinate, t time, u_i velocity, e specific total energy, σ_{ij} a stress tensor and f_i the external body force per unit mass.

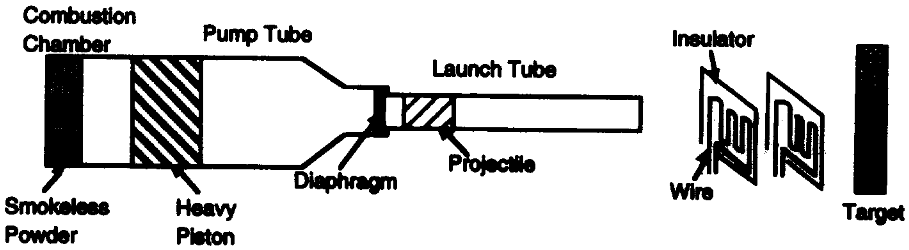

Fig. 2. Schematic diagram of two-stage light-gas gun accelerator system.

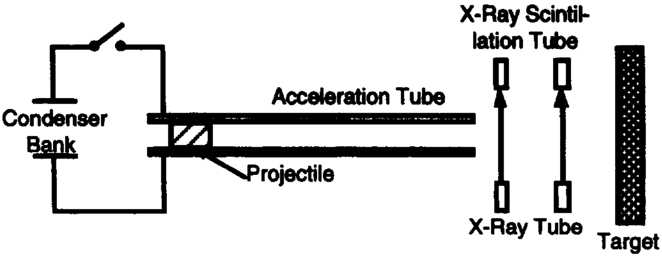

Fig. 3. Schematic diagram of rail gun accelerator system.

The subscripts refer to tensor components and Einstein's summation convention is implied by the repeated indices.

The two methods are depicted schematically in Fig. 4. In the Lagrangian frame of reference the vertices of the grid move with the local flow velocity, and material initially within a cell remains in that cell. Compared with the Eulerian method this formulation is computationally more economical and, since no convection of material occurs, it can easily and accurately track free surfaces, material interfaces and history-dependent material behavior. The major disadvantage of this formulation is that if excessive deformation occurs, the calculation grid can become so distorted that the solution becomes inaccurate and the problem has to be terminated prematurely owing to the limitation of the Courant condition. In order to cope with this problem, especially to solve the perfect penetration process, it is necessary to make use of the rezoning capability. Also impact/slide interfaces between two grids are also indispensable to impact analysis.

On the other hand, in the Eulerian frame of reference the vertices of the grid stay fixed in space while material is convected from cell to cell. Therefore, the Eulerian formulation has no problem handling large deformations and fluid flow, although it is more difficult to track free surfaces, material interfaces and history-dependent material behavior and is subject to numerical diffusion associated with material convection. Multiple material capability is indispensable to impact analysis in this formulation.

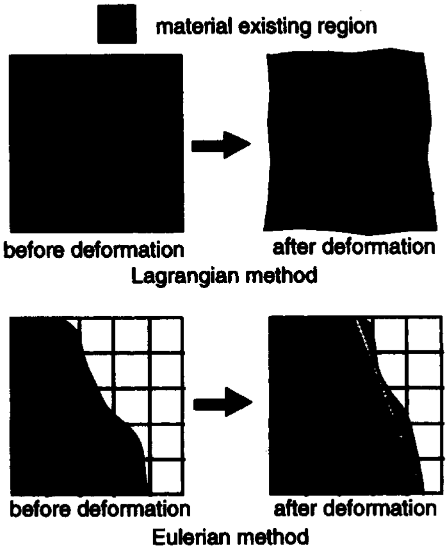

Fig. 4. Schematic diagrams of comparison between the Lagrangian and Eulerian methods.

4. NUMERICAL OPTIMIZATION OF MATERIAL MODELS

4.1. Numerical modeling

A two-dimensional hydrocode based upon an explicit finite difference method, AUTODYN-2D™, was used in the present study overall [5]. For the single target impact analyses and the final stage analyses, the Eulerian frame of reference was applied, while the Lagrangian frame of reference was applied for the impact analysis against the Whipple bumper shield at the middle stage. In the former formulation the multiple material capability enables us to calculate the interaction between different materials without complicated manual procedures.

Since the impact process against the thick target is a more complicated phenomenon than that against the thin target, a parametric study was performed and compared with the experimental results for the thickest target (38.9 mm) modeling the main wall. In this program, as many hydrocodes do, the material model consists mainly of two parts: (1) the equation of state describes the relation among pressure, density and internal energy and (2) the material strength model does the constitutive relation including a failure model.

The Mie–Grüneisen form of the shock Hugoniot equation of state was applied for all materials in this study. It has been known that a linear relationship between the shock velocity (U_s) and the particle

Table 1. Material properties of projectiles

Material property	Polycarbonate	Polyethylene
Equation of state	Shock Hugoniot	Shock Hugoniot
Density (g cm^{-3})	1.196	0.9506
c_0 (cm μs^{-1})	0.1933	0.305
s (–)	3.49	1.328
Grüneisen γ (–)	0.61	0.67
Material strength model	Hydrodynamic	Hydrodynamic

Table 2. Material properties of targets

Material property	2024-T351 Al
Equation of state	Shock Hugoniot
	$\rho = 2.785$ g cm^{-3}
	$c_0 = 0.5328$ cm µs^{-1}
	$s = 1.338$ (–)
	$\gamma = 2.0$ (–)
	$C = 0.875$
	$T_{room} = 300$ K
Material strength model	Johnson–Cook
	$G_0 = 0.276$ Mbar
	$A = 2.65$ kbar
	$B = 4.26$ kbar
	$n = 0.34$ (–)
	$C = 0.015$ (–)
	$m = 1.0$ (–)
	$T_{melt} = 775$ K

velocity (u_p), as shown below, can adequately represent the Hugoniot for many materials which impact at velocities less than the threshold for shock-induced vaporization.

$$U_s = c_0 + su_p \tag{1}$$

where c_0 and s are experimentally determined material constants and c_0 denotes the bulk sound velocity.

The material strength models for both high density polyethylene and polycarbonate were assumed to be hydrodynamic. For 2024-T3 aluminum the Johnson–Cook model was applied [6]. This model is considered to be suitable for high-strain rate deformation and highly non-linear behavior depending on pressure, density, strain and temperature changes. In the Johnson–Cook model the shear modulus (G_0) is assumed to be constant and the yield stress strength is expressed as

$$Y = (A + B\varepsilon^n)(1 + C \ln \dot{\varepsilon})(1 - T^{*m}) \tag{2}$$

where ε is the effective plastic strain, $\dot{\varepsilon}$ the effective plastic strain rate (s^{-1}) and T^* is homologous temperature,

$$T^* = \frac{T - T_{room}}{T_{melt} - T_{room}} \tag{3}$$

where T is the absolute temperature and subscripts room and melt denote room and melting temperatures respectively. The quantities A, B, C, m and n are the material constants determined by experiments.

Two sorts of failure criteria were applied: the hydro tensile limit and ultimate strain. These are based upon the instantaneous failure model for field variables. In the former model the failure is triggered by the appearance of the maximum tensile (or negative) hydrostatic pressure (P_{min}), and in the latter model by the maximum effective plastic strain (ε_{max}). These two models enable us to simulate approximately the spallation type fracture and large strain ductile hole formation fracture, respectively. The material properties of the projectiles and the targets used in this study are listed in Table 1 and Table 2 respectively. In the experiment the 2024-T3 aluminum alloy was used for the target material in every case, but there are reported no material properties of Johnson–Cook models for itself. Those for 2024-T351 aluminum were used in place of 2024-T3 aluminum for each model.

Since the two kinds of projectile materials have comparable shock impedances and can be considered to be hydrodynamic as compared with the target material, the differences in the projectile materials in themselves do not have very significant effects upon the deformation and fracture behaviors of the targets. It might depend mainly upon the initial kinetic energies and the shapes of the projectiles in the present study.

In this parametric study we determined the most suitable values of P_{min} and ε_{max} for the 2024-T3 aluminum in addition to the material properties shown in Table 2. As the first step these values were benchmarked by comparing the calculated results

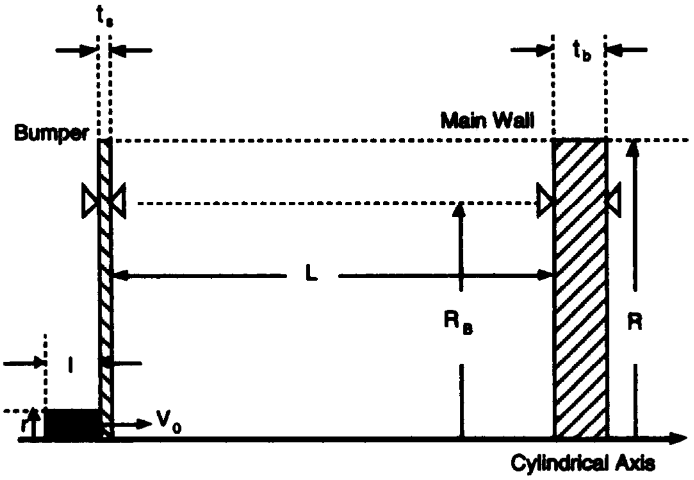

Fig. 5. Geometry of numerical analysis.

Table 3. Calculational conditions of the parametric study

	Projectile					Target	
Case name	Material	Mass (g)	Length (mm)	Radius (mm)	Velocity (km s^{-1})	Radius (mm)	Thickness (mm)
CASE-1	Polycarbonate	0.94	10.0	5.0	7.45	124	38.9
CASE-2	Polycarbonate	0.94	10.0	5.0	7.06	124	22.2
CASE-3	Polyethylene	3.65	24.1	7.1	3.99 [a]	124	38.9
CASE-4	Polyethylene	3.65	24.1	7.1	3.99 [a]	124	22.2
CASE-5	Polyethylene	14.0	30.0	12.5	2.16	124	38.9
CASE-6	Polyethylene	14.0	30.0	12.5	2.16	124	22.2

[a] Measured by a separate test.

with the final profile of the first target for an experimental condition.

Figure 5 shows the geometric configuration of the numerical analysis modeled by a two-dimensional axisymmetric approach. In the experiment the targets are square, but in the calculation they are assumed to be circular plates with equivalent sectional areas. Although this figure includes two targets, a bumper and a main wall, only the first target is an object of these preliminary calculations. The displacement of every target is constrained in all directions at the circular plane about 105 mm distant from the axis in

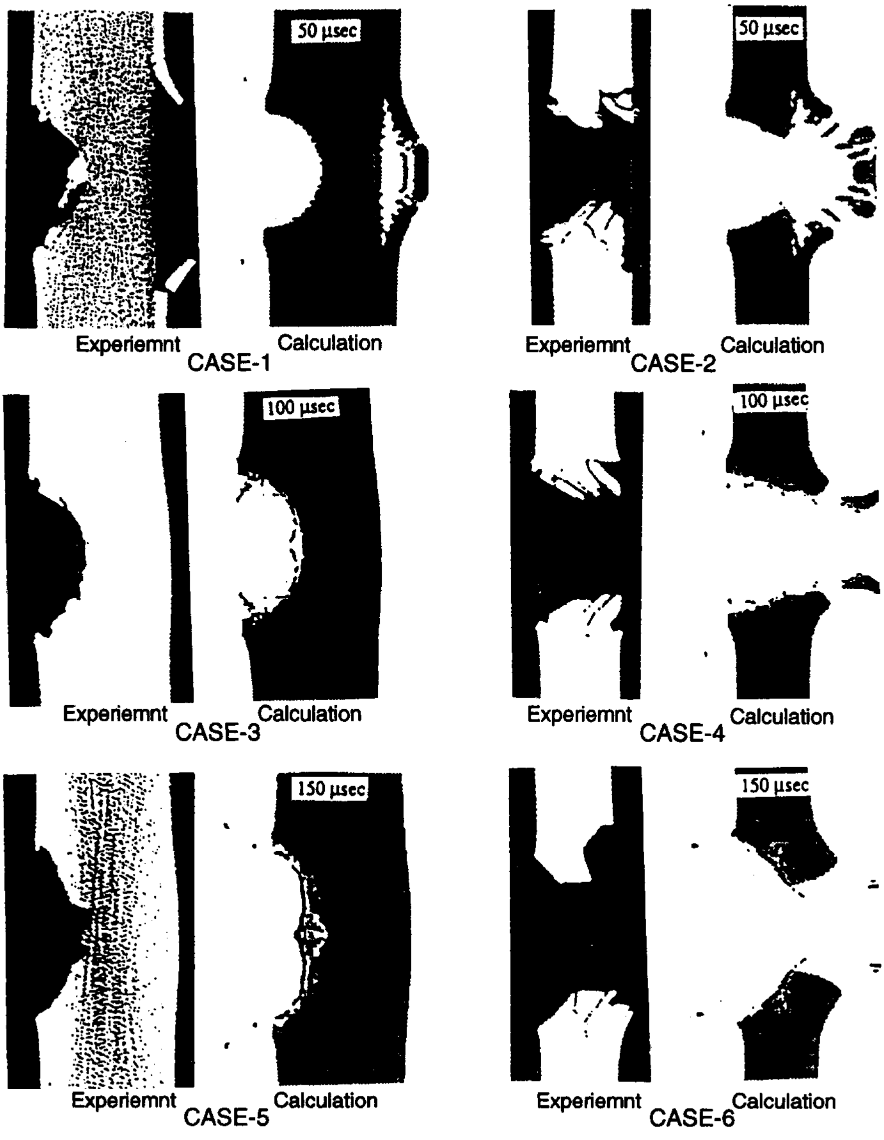

Fig. 6. Comparison of the final target profiles between experiments and calculation.

Table 4. Failure parameters of 2024-T3 aluminum used in each calculation

Impact velocity	P_{min} (Mbar)	$\varepsilon_{\mathrm{max}}$ (–)
ISAS (CASE-1, 2)	– 0.015	2.0
Tohoku Univ. (CASE-3, 4)	– 0.012	1.0
Kyoto Univ. (CASE-5, 6)	– 0.012	0.5

Table 5. Main Parameters for the Whipple Bumper Impact Simulations by Space Debris

Case name	Bumper thickness t_s (mm)	Impact velocity V_0 (km s^{-1})
CASE-A	2.5	1.93
CASE-B	4.8	2.16
CASE-C	12.7	1.97
CASE-D	22.2	2.16

order to model the actual bolt-on constraint, but this boundary condition is applied so that the pressure wave can travel away through the plane in the radial direction.

4.2. Parametric calculations

About twenty cases of calculations using the different pairs of P_{min} and $\varepsilon_{\mathrm{max}}$ were carried out for the condition of CASE-1 shown in Table 3. This condition corresponds to the case with the highest impact velocity and the thickest target. Through these parametric calculations the results using $P_{\mathrm{min}} = -0.015$ Mbar (= 1.5 GPa), $\varepsilon_{\mathrm{max}} = 2.0$ showed the best agreement with the experiment, and any result using -0.012 to -0.020 Mbar for P_{min} is in fair agreement with the experimental result, while the spallation fracture did not occur in case of $P_{\mathrm{min}} = -0.030$ Mbar, for example. It should also be noted that the result using the elastic–perfectly-plastic model was ascertained to indicate a significant difference from the experiment by another test calculation.

Then we performed similar calculations for the other five cases in Table 3 using the material properties of 2024-T3 aluminum determined through the above procedure: $P_{\mathrm{min}} = -0.015$ Mbar, $\varepsilon_{\mathrm{max}} = 2.0$ for the Johnson–Cook model. The calculated result of CASE-2 indicated a fairly good agreement with the experimental result, but the result for CASE-6 estimated the perforated diameter as much smaller than that in the experiment, especially in the rear of the target. Although the other results were not so different from the experiments, both depths and diameters of the craters in the front of the targets were smaller than the experiments. In order to resolve these problems we carried out more test calculations for CASE-2 through CASE-6 again using several different pairs of P_{min} and $\varepsilon_{\mathrm{max}}$ together with the Johnson–Cook model. Those results indicated that a value smaller than 2.0 should be used for $\varepsilon_{\mathrm{max}}$ for CASE-3 through CASE-6. For both CASE-5 and CASE-6 tested by the slowest impact velocities, the calculated results using $\varepsilon_{\mathrm{max}} = 0.5$ showed the best agreement with corresponding experimental results. This is coincident with the fact that the static fracture strain of the aluminum alloy is about 50%. Generally speaking, the tendency of the effects of the P_{min} and strength models upon the final profiles of targets for the cases except for CASE-1 was similar to that of CASE-1. Figure 6 depicts the comparison of the final target profiles between the experimental results and the calculated results which showed the best agreements with the corresponding experimental results for CASE-1 through CASE-6. In all these calculations the Johnson–Cook strength model was used together with the pairs of $\varepsilon_{\mathrm{max}}$ and P_{min} values as shown in Table 4. Every calculated result simulates the basic deformation or fracture geometry in the experiment, sufficiently well from a qualitative viewpoint and fairly well quantitatively. In the case of the thinner target we can see for both experimental and calculated results that the higher the impact velocity becomes, the more the shapes of perforated targets are bent backward like a petaling phenomena.

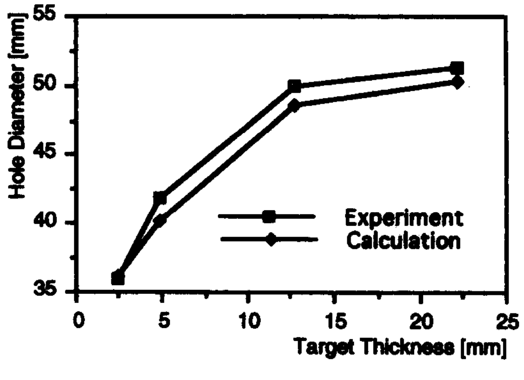

Fig. 7. Comparison between the experimental and calculated results for the target thickness vs. the perforated hole diameters.

For the purpose of a further verification of this material model we performed three more calculations modeling the single target perforation process. Every case has the same impact velocity (2.16 km s^{-1}, corresponding to the slowest impact velocity in the present study) but three different target thicknesses: 2.5, 4.8 and 12.7 mm. We have the experimental results for these cases obtained by using the powder gun of Kyoto Univ. Also, the above-mentioned CASE-6 corresponds to a thicker target test which was also perforated completely by the same type of

Table 6. Calculational conditions of the Whipple bumper impact simulations by space debris

Properties	Values
Projectile material	Polyethylene
length: l (mm)	30.0
radius: r (mm)	12.5
Main wall material	2024-T3 Al
thickness: t_b (mm)	38.9
radius: R (mm)	124.0
fixed radius: R_B (mm)	105.0

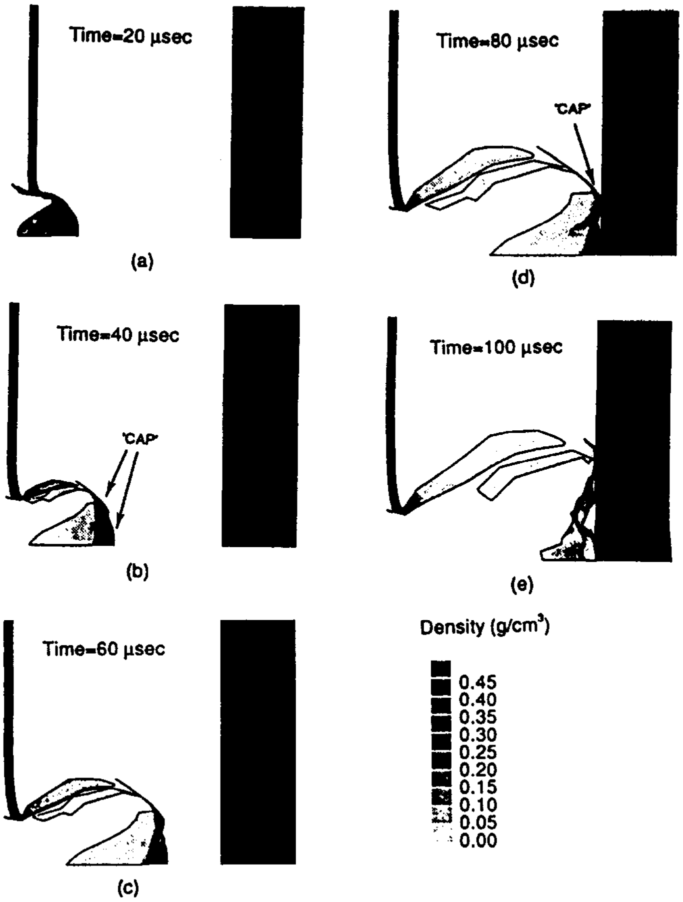

Fig. 8. Density contours by the interactive Lagrangian rezoning method: CASE-B.

projectile. Figure 7 shows the relation of the target thickness to the perforated diameter for these four cases, comparing the calculations with the experiments. These results also indicate a good agreement between the experiment and the calculation. The reason why hole diameters increase as target thicknesses increase is that the projectiles tend to deform to a greater degree and to create larger holes as the targets become thicker.

As we have seen above, our material model has been successfully verified to be applicable for the analysis of the cratering and perforation process of the aluminum target by the plastic projectile.

5. LAGRANGIAN APPROACH TO THE WHIPPLE BUMPER IMPACT ANALYSIS

On the basis of the investigations in the previous section a series of numerical simulations were performed by using an interactive Lagrangian rezoning method. Although this method still forces us to do more time-consuming procedures than the multiple material Eulerian method, but it is much easier to use than conventional manual rezoning procedures. The Lagrangian approach is expected to provide us with more accurate material boundary configurations. At the same time this method can save markedly on both the computer CPU time and memory in comparison with manual procedures. In another paper, we ascertained the mutual agreement of the results calculated by these two methods [4].

This time Fig. 5 fully represents the calculation system in this section. Four cases of calculations were carried out to simulate the experiments made at Kyoto Univ., as shown in Table 5. Every bumper material is composed of 2024-T3 aluminum. The other parameters are the same for all cases, as listed in Table 6. The boundary conditions applied on both targets are the same as those mentioned in the previous section. The Johnson–Cook strength model was applied to all the calculations together with the instantaneous failure criteria $P_{\min} = -0.012$ Mbar and $\varepsilon_{\max} = 0.50$.

Figure 8 depicts the process of debris cloud formation created by the bumper perforation expanding toward a main wall and impacting it for CASE-B in Table 5. This Figure shows that the density in the debris cloud is no more than 0.10 g cm^{-3} everywhere at the instance of a second impact but that the "cap" lay ahead of the debris cloud made from the bumper material, shaped like a bowl with a thick and flat base in Fig. 8(c) and (e), still has a higher density than the cloud made from both the projectile and target materials. This low density in the debris cloud region might be regarded as the average density; that is, most of the projectile and the part of the target fractured by the sharing force were fragmented into small pieces judging from the impact velocity. On the other hand, the "cap" can be considered to retain a few lumps. We recognize that the "cap" composed of these lumps causes the main wall to deform in a complicated manner rather than the debris cloud does. It should be carefully noted that in this figure some fragments after damaging the main wall were removed from the calculation system by the rezoning procedure in order not to affect the time step of the explicit solution scheme. These figures demonstrate the mechanism by which the "cap" made from the bumper material mainly creates a crater in the front of the main wall in double or triple rings.

Figure 9(a), (b) shows the comparison of the final profiles of the main walls between the experiment and the interactive rezoning calculation by Lagrangian method for CASE-A and CASE-B, respectively. As there existed no significant damage of main walls in the results of both the experiment and the calculation for CASE-C and CASE-D, those results are not reported here. The calculated results for CASE-A and CASE-B are in fairly good agreement with the corresponding experimental results in the shape of multiple ring craters. However, the calculated results overestimate the swelling in the rear side, caused by spalling, as compared with the experiment.

The calculated energy balance histories for four cases are shown in Fig. 10. In this Figure PROJ, TARG1 and TARG2 stand for a projectile (debris), a first target (bumper) and a second target (main wall) respectively, and Int.Energy and Kin.Energy stand for the internal energy and the kinetic energy respectively. From the comparison of these four graphs we can understand that the thicker a bumper becomes, the more rapidly does a projectile decrease its kinetic energy and the more internal energy does a bumper absorb. CASE-A and CASE-B come to stable equilibrium earlier than CASE-C and CASE-D do, because these two projectiles lose only a little kinetic energy during the impact against the bumpers and the debris clouds expand with the higher velocities. The drastic changes around 75 ms in the results for CASE-A and CASE-B represent the impacts of debris clouds against the main walls. As mentioned for the previous figure, we also recognize from these figures that the energy absorptions by the main walls are very small for CASE-C and CASE-D.

6. EULERIAN APPROACH TO THE WHIPPLE SHIELD IMPACT ANALYSIS

We performed the calculations of the same problems shown in the previous section using the multiple material Eulerian method again. This was

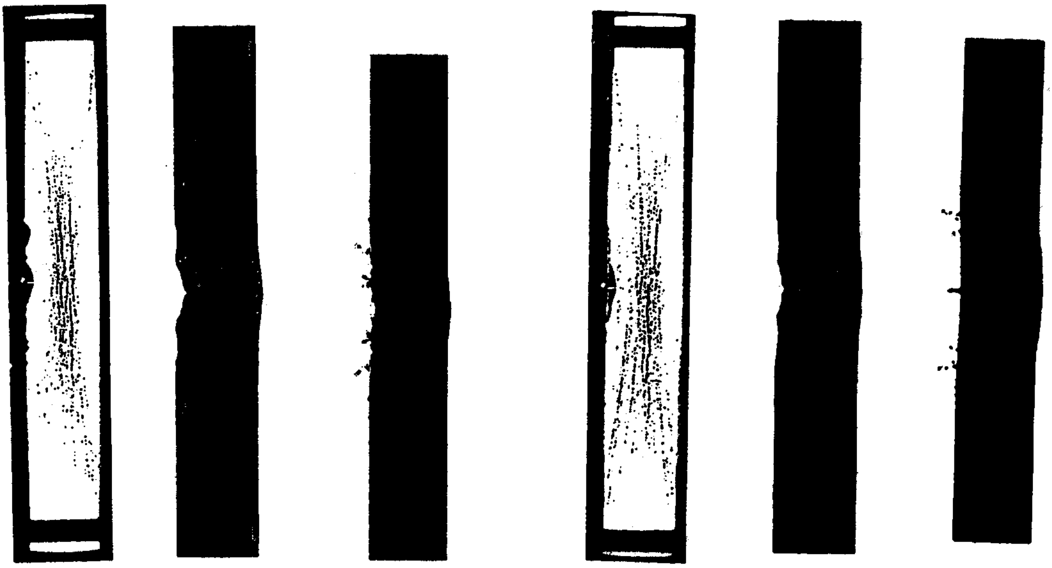

Experiment (a) | Lagrangian Calculation (b) | Eulerian Calculation (c)
CASE-A

Experiment (a) | Lagrangian Calculation (b) | Eulerian Calculation (c)
CASE-B

Fig. 9. Comparison of the final profiles of the back wall.

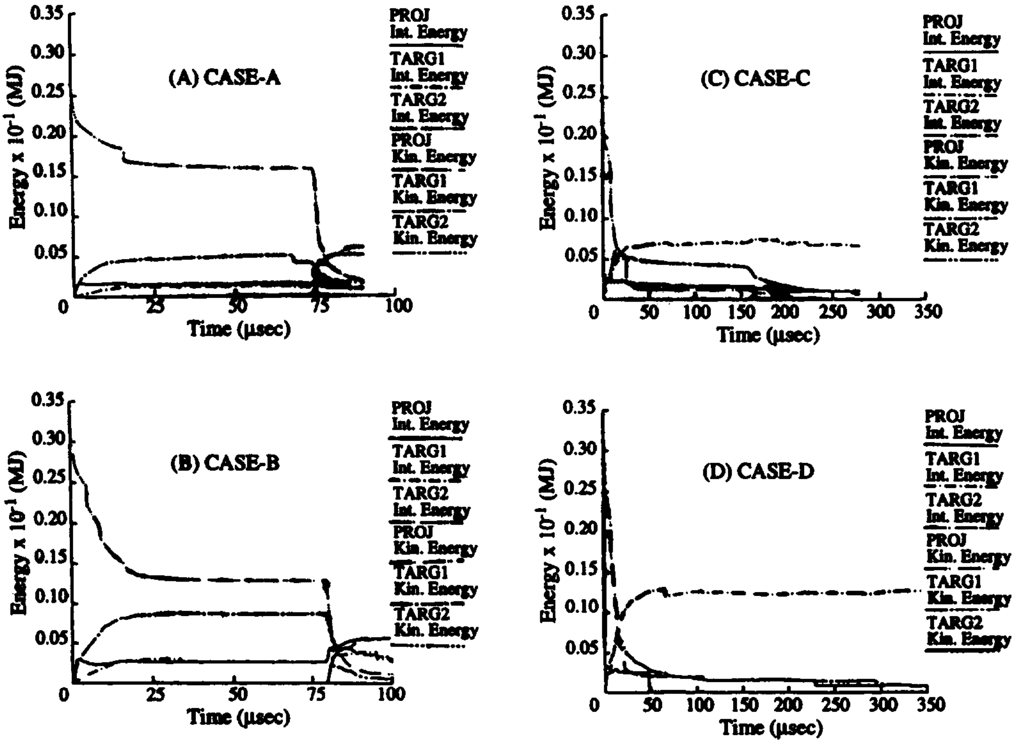

Fig. 10. Energy balance histories of CASE-A through CASE-D in the Lagrangian calculation.

partly because this method is much easier to use for almost all users, and boundary configurations. At the same time this was partly because the remarkable advance in computer hardware in recent years has enabled us to carry out a calculation of such a size without a special supercomputer.

Figure 11 indicates the comparison of the calculated results for the interactive Lagrangian rezoning and multiple material Eulerian methods for CASE-B. Figure 9 also shows the comparison of the final target profiles obtained by the same series of calculations for CASE-A and CASE-B. They are in fairly good agreement with each other.

7. DISCUSSION AND CONCLUSIONS

Two kinds of instantaneous fracture models were tested for adaptability to hyper- and high-velocity impact analyses, combining the shock Hugoniot equation of state and the Johnson–Cook strength model. For the analyses of the hypervelocity or ultrahigh-velocity impact problems in which the shock-induced vaporization occurs for impacts of over 10 km s^{-1} velocity, the equation of state has a great apparent importance, while the material strength model may be of little importance. However, for slower impact problems it is recommended to apply the constitutive models taking account of the effects of work-hardening, strain rate hardening, thermal softening and melting.

Through the present study it was made clear that the fracture criteria of a target material are highly dependent on the impact velocity, especially in regard to the ductile hole formation process. Essentially the dynamic fracture model should be dependent upon various field variables such as the constitutive model. In addition the loading history to which a portion of the material has been subjected is known to have a great importance in the fracture mechanism. Actually a number of ideas have been proposed by different researchers. It is reported that the consideration of duration time yields better results than a simple instantaneous fracture model for spallation type fracture [7]. In more sophisticated models the damage function is dependent upon several field variables which gradually accumulate the damage degradation of the material, and the failure is triggered when the value of the function attains 1.0 [8]. However, it is not too much to say at present that they have not been tested sufficiently by the experiment for the wide range of the impact velocities and various materials. Therefore, our proposed analysis method, although using simplified failure models, provides a useful tool with fairly good accuracy for the purpose of predicting space debris impact problems against Whipple bumper shield. Moreover, it helps us to comprehend the mechanism of various types of cratering and perforation phenomena such as spallation, petaling and single or multiple hole formation ductile fracture. In particular, the Lagran-

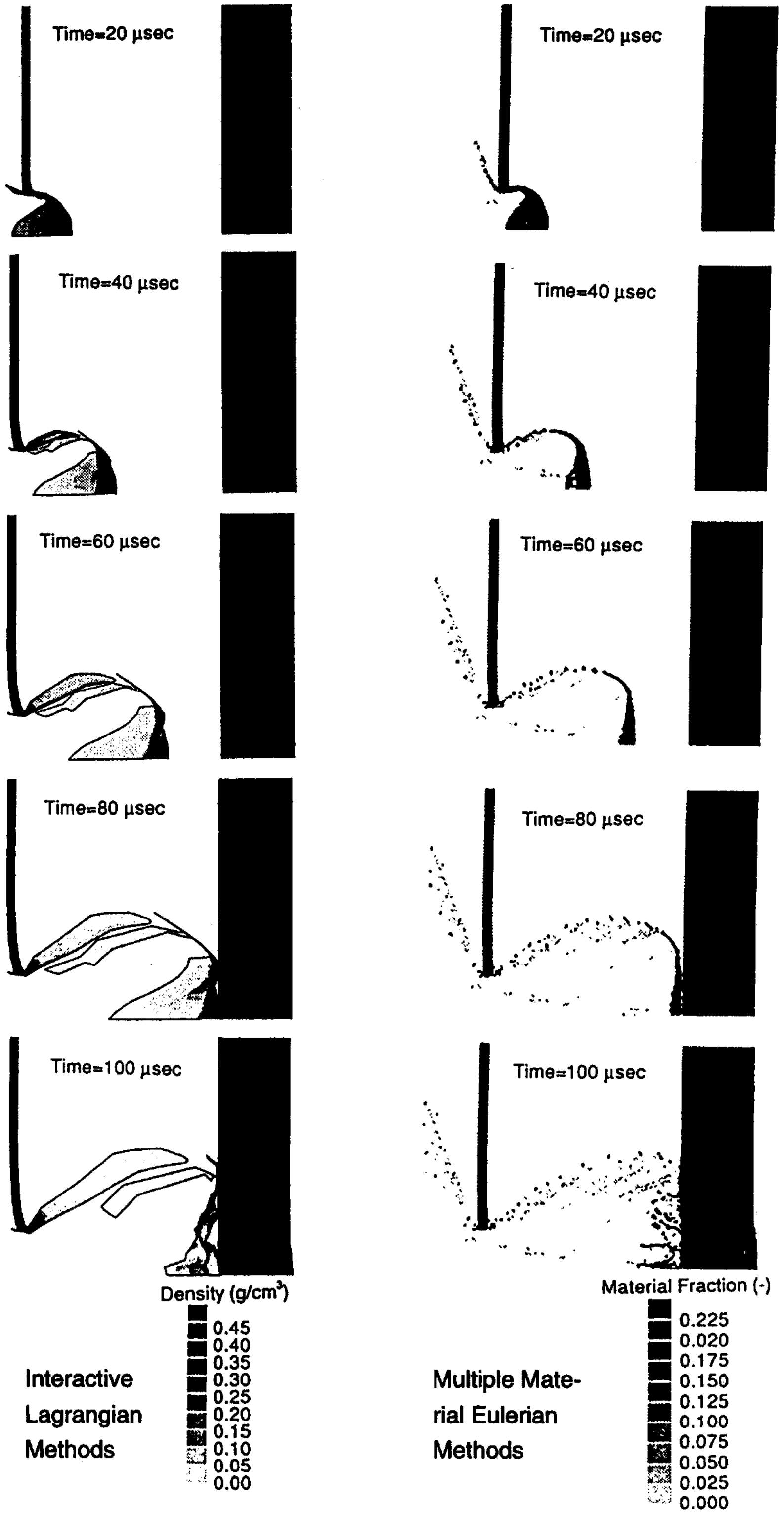

Fig. 11. Comparison of the calculated results for the interactive Lagrangian and the multiple material Eulerian methods.

gian approach provides such a clear material boundary that we can determine the detailed process of debris cloud expansion and main wall impact. On the other hand, with the Eulerian approach we can obtain the overall impact simulation result of the Whipple bumper shield by space debris without complicated manual procedure.

Acknowledgements—The authors gratefully acknowledge Prof. T. Kurokawa of Kyoto University, Prof. K. Takayama of Tohoku University, Prof. J. Onoda and Prof. N. Kawashima of the Institute of Space and Astronautical Science, who kindly provided the authors with the opportunities to utilize their excellent hypervelocity impact test facilities. The authors would also like to express their gratitude to Mr. Sugimoto of the National Aerospace Laboratory for his cooperation in the X-ray CT scanning system operation. Lastly we also thank Mr. T. Ohta of the CRC Research Institute for his persevering performance of interactive rezoning procedures by a hydrocode.

REFERENCES

1. Kibe, S., Toda, S. and Katayama, M., A study between hypervelocity impact test results and numerical simulation using a hydrocode. In *44th Congress of the International Astronautical Federation*, Graz, Oct. 1993, IAF-93-1.4.239.
2. Katayama, M., A numerical simulation of hypervelocity impact problem by a hydrocode. In *Proc. Space Debris Workshop* '91, Sagamihara, Japan, Nov. 16, 1991. The Institute of Space and Astronautical Science (ISAS), Sagamihara, Japan, 1991, pp. 33–38.
3. Katayama, M., Aizawa, T., Kibe, S. and Toda, S., A numerical simulation of hypervelocity impact of space debris against the Whipple bumper system. In *Proc. 1st European Conf. on Space Debris*, Darmstadt, Germany, April, 1993. The European Space Agency (ESA), Darmstadt, Germany, 1993, pp. 419–424.
4. Wilkins, M. L., Calculation of elastic–plastic flow. Lawrence Livermore Laboratory Report, UCRL-7322, revision 1, 1973.
5. Robertson, N. J., Hayhurst, C. J. and Fairlie, G. E., Numerical simulation of explosion phenomena. *Int. J. Comput. Appl. Technol.* 1994, 7(3–6), 316–329.
6. Johnson, G. R. and Cook, W. H., A constitutive model and data for materials subjected to large strains, high strain rates and high temperatures. In *Proc. 7th Int. Symp. on Ballistics*, The Hague, The Netherlands, 1983. International Ballistic Committee, The Hague, The Netherlands, 1983, pp. 541–547.
7. Tuler, F. R. and Butcher, B. M., A criterion for the time dependence of dynamic fracture, *Int. J. Fract. Mech.*, 1968, **4**, 431–437.
8. Johnson, G. R. and Cook, W. H., Fracture characteristics of three metals subjected to various strains, strain rates, temperatures and pressures, *Eng. Fract. Mech.*, 1985, **21**, 31–48.